# Near-Unity Chiral Terahertz Generation Driven by Asymmetric Quasi-Bound States in the Continuum

Xueying Yao(姚雪盈)[1], Zirui Guo(郭子瑞)[1], Yanxue Hou(侯岩雪)[1], Cai Luo(罗猜)[1], Ruiqi Yao(姚瑞琪)[1], Jianmei Li(李健梅)[1**], Guilin Wen(文桂林)[2**]

[1]Key Laboratory for Microstructural Material Physics of Hebei Province, School of Science, Yanshan University, Qinhuangdao 066004, China.

[2]School of Mechanical Engineering, Yanshan University, Qinhuangdao 066004, China.

This work was supported by the Key Program of National Natural Science Foundation of China, Grant Nos.12332002; This work was also supported by the Program of China Scholarship Council (Grant No. 202407810013).

****Corresponding author. Email:** jianmeili@ysu.edu.cn (J. Li) and glwen@ysu.edu.cn (G. Wen).

**Abstract:**

Efficient generation of terahertz (THz) radiation with both high emission strength and near-unity chiral purity remains a central challenge in nonlinear chiroptics. Here, we numerically demonstrate a framework for chiral THz generation from asymmetric lithium niobate (LN) metasurfaces enabled by chiral quasi-bound states in the continuum (q-BICs). By simultaneously breaking in-plane and out-of-plane symmetries, structural chirality is directly transferred to the optical-rectification process, enabling deterministic control of nonlinear THz emission. The resulting metasurface achieves a full-spectrum averaged THz circular dichroism (CD) of 0.99, while maintaining THz emission amplitudes comparable to nonlinear metasurface emitters under 100 fs excitation. The same symmetry-engineered mechanism yields an SHG-CD of 0.99, confirming the robustness of the nonlinear chiral response. In addition, the platform supports dynamic spectral tuning through pump-pulse engineering without sacrificing strong chiral selectivity. These results establish chiral q-BICs as a general strategy for engineering nonlinear chiro-optical interactions and provide a scalable route toward chip-integrated chiral THz photonic devices based on the lithium-niobate-on-insulator (LNOI) platform.

**Keywords:** Terahertz; Lithium niobate; Metasurfaces; Circular dichroism; Bound states in the continuum

**PACS:** 74.70.Dd, 74.25.Fy, 74.25.Ha, 74.62.-c



This work was supported by the Key Program of the National Natural Science Foundation of China (Grant No. 12332002) and the China Scholarship Council (Grant No. 202407810013).

## 1. Introduction.

Chiral electromagnetic responses play a central role in light-matter interactions[1-4] involving spin angular momentum and are essential with applications in enantiomer discrimination[5], molecular spectroscopy[6], and polarization-resolved imaging[7]. Extending chirality into the terahertz (THz) regime is of particular importance, as THz radiation[8, 9] probes low-energy excitations in molecules and condensed matter systems, offering unique sensitivity to structural and dynamical properties[10]. Recent advances in THz metasurfaces have enabled circular dichroism (CD), asymmetric transmission[11], and polarization manipulation[12, 13]through subwavelength structural engineering. These approaches primarily operate in the linear regime, where chirality is imposed on incident radiation rather than generated intrinsically. Chiral THz emission has been demonstrated in spintronic heterostructures and quantum materials, where ultrafast spin currents, inverse spin Hall effects, and photogalvanic or spin-orbit-coupling-induced mechanisms generate polarization-controlled THz radiation[14-17]. For example, metasurface-integrated spintronic emitters can produce broadband THz waves with tunable chirality[14]. Nevertheless, these approaches rely on material-specific electronic processes rather than structurally engineered photonic chirality, and often require complex magnetic multilayers, limiting scalability and design flexibility for photonic integration.

All-dielectric metasurfaces provide an alternative route for manipulating and generating THz radiation through engineered optical responses. In particular, optical rectification, a second-order nonlinear process, has been widely employed for broadband THz generation in bulk crystals[18-20] and nanostructures[21, 22]. Resonant dielectric metasurfaces can significantly enhance local electromagnetic fields and improve THz generation efficiency, enabling compact and efficient THz emitters[23, 24]. As a result, the generated THz radiation in such systems is typically linearly polarized or only weakly dependent on the circular polarization of the excitation, as the nonlinear emission process is not intrinsically coupled to structural chirality.

This limitation highlights a central challenge of directly encoding chirality into nonlinear emission within a purely photonic platform. Bound states in the continuum (BICs)[25-27] support high quality (Q) factor resonances through symmetry protection, enabling strong field

confinement and enhanced light-matter interactions. By introducing symmetry breaking, quasi-BIC (q-BIC) modes allow controlled radiation coupling while preserving large field enhancement, which is essential for nonlinear optical processes [28-32]. Symmetry engineering further enables selective coupling to circularly polarized states, giving rise to pronounced chiral responses with near-unity circular dichroism[33-37]. Recent advances in nonlinear chiral metasurfaces have demonstrated that resonant dielectric platforms, including q-BIC systems, can simultaneously enhance nonlinear optical processes and enable pronounced chiral responses [38, 39]. Yet their role in directly linking nonlinear THz generation with intrinsic chirality remains unresolved.

Realizing such a mechanism requires a material platform that simultaneously supports strong second-order nonlinearity and scalable photonic integration. Lithium niobate (LN)[40-42] provides a suitable candidate due to its large second-order nonlinear susceptibility and broad transparency window spanning from the visible to the terahertz regime. More importantly, the development of thin-film lithium niobate on insulator (LNOI) has enabled wafer-scale fabrication of low-loss, high-confinement photonic structures, establishing LN as a versatile integrated photonic platform capable of supporting complex on-chip functionalities[43-45]. Recent advances have demonstrated that LN photonic circuits can achieve high-efficiency nonlinear conversion, ultrafast modulation, and scalable integration, positioning LN as a promising platform for nonlinear and active nanophotonics beyond conventional silicon-based systems[29, 46, 47].

Despite these advances, translating the extreme field enhancement and linear chiral selectivity of three-dimensional q-BICs into the nonlinear regime remains a significant challenge, particularly in the THz regime. The difficulty lies in efficiently mapping symmetry-governed mode characteristics onto nonlinear source terms to dictate emission dynamics while reconciling radiation power with polarization purity. This physical gap hinders the realization of high-performance chiral THz sources that maintain strict selectivity across broad spectral bandwidths.

In this Letter, we demonstrate an asymmetric LN metasurface supporting a chiral q-BIC resonance for nonlinear THz generation. The simultaneous breaking of in-plane and out-of-plane symmetries enables strong polarization selective coupling and efficient nonlinear

emission. The dual symmetry breaking produces circular-polarization-selective q-BIC coupling at the pump wavelength, so that the resonantly enhanced $E_z$ field drives a strongly asymmetric second-order nonlinear polarization and, consequently, chiral THz generation. In the following, we systematically investigate the chiral response, nonlinear THz emission, and dynamic tunability of the proposed metasurface.

## 2. Results

### 2.1 Metasurface Design and Nonlinear Excitation Scheme.

The proposed chiral metasurface and its operational principles are delineated in Fig. 1. As schematically illustrated in Fig. 1(a), the proposed metasurface facilitates chiral-selective coupling to q-BIC, enabling asymmetric local field enhancement. The unit cell geometry, shown in Fig. 1(b), consists of x-cut LN nanorod dimers arranged in a square lattice with the optical axis (c-axis) aligned along the laboratory z-axis. The rectangular prism nanorods are characterized by their length (L), width (w), and height (H). In this x-cut configuration, the incident field component $E_z$, which drives the dominant $d_{33}$ nonlinear response, interacts with the extraordinary refractive index ($n_e \approx 2.21$ at 640 nm), while the $y$-component experiences the ordinary index ($n_o \approx 2.28$).The entire structure is supported on top of a silicon dioxide layer (n = 1.45). These real-valued refractive indices are used in the present transient model. The resulting transient fields are subsequently analyzed via Fourier transform to extract the spectral components across the fundamental, harmonic, and THz regimes.

In the present transient model, the second-order response is treated using an instantaneous effective $\chi^{(2)}$, while the subsequent discrete Fourier transform (DFT) is employed only to extract the frequency-domain spectrum from the calculated time-domain fields. Frequency-dependent linear and nonlinear material dispersion from the optical to THz regime are therefore not explicitly included. This approximation may affect the absolute THz amplitude and detailed spectral weighting, particularly at higher THz frequencies. Accordingly, the calculated THz spectra are interpreted primarily in terms of the q-BIC-induced polarization contrast and structural trends rather than as absolute material-limited prediction of THz output. Because the same material model is applied to both LCP and RCP excitation, the relative polarization

contrast is expected to be less sensitive to these common material-dispersion effects than the absolute THz amplitude.

By simultaneously introducing an in-plane rotation θ and an out-of-plane height disparity $\Delta h$, the intrinsic mirror symmetries are broken, driving the transition from a symmetry-protected BIC to a radiative q-BIC mode characterized by a pronounced chiral response. For the precise modeling of transient nonlinear dynamics, the metasurface is illuminated by a normally incident, spatiotemporally modulated ultrafast Gaussian pulse. Following the software's vectorial representation for LCP (+) and RCP (−) excitation along the x-direction, the incident electric field is expressed as

$$\boldsymbol{E}_{\pm}(x,y,z,t) = Re\left\{E_0\sqrt{\frac{w_0}{w(x)}}exp\left[-\frac{y^2+z^2}{w^2(x)}\right]exp[i\Phi(x,y,z,t)]exp\left[-\frac{(t-t_0)^2}{dt^2}\right]\hat{\boldsymbol{e}}_{\pm}\right\} \quad (1)$$

where $w(x)$ is the beam radius, $\Phi(x,y,z,t)$ incorporates the phase evolution and wavefront curvature. The pulse follows a temporal Gaussian envelope centered at $t_0 = 0.5$ ps with a temporal width $dt = 100fs$. The polarization vectors are defined as $\hat{\boldsymbol{e}}_{\pm} = (\hat{\boldsymbol{y}} \pm i\hat{\boldsymbol{z}})/\sqrt{2}$, corresponding to left- and right-circular polarization (LCP/RCP), respectively. This complex formulation accounts for diffraction effects and temporal oscillations essential for high-fidelity simulation. The excitation is accurately modeled using spatiotemporally modulated Gaussian pulses, with the full vectorial expression detailed in Supplementary S1.1. The nonlinear response in LN is dictated by the second-order susceptibility tensor $\chi^{(2)}$. Under the x-cut configuration, the response is dominated by the $d_{33}$ coefficient. Consistent with the ferroelectric crystallographic convention and to account for dispersive enhancement at the 640 nm excitation wavelength, we set $d_{33} = -38$pm/V[48]. The resulting second-order nonlinear polarization along the optical axis is

$$P_z^{(2)}(t) \approx \varepsilon_0 d_{33} E_z^2(t) \quad (2)$$

This induced polarization serves as the driving source for both harmonic generation and broadband THz emission. As illustrated in the frequency-domain representation in Fig. 1(c), the optical rectification process can be interpreted through energy conservation: pairs of frequencies $\omega_0 \pm \Delta\omega$ from the pulse's finite bandwidth coalesce to generate low-frequency radiation at $\Omega = 2\Delta\omega$. In the time domain, this manifests as a slowly varying component proportional to the intensity envelope $E^2(t)$, directly translating to THz emission whose

bandwidth is inherently determined by the pulse duration.

Numerical simulations were conducted using the finite element method with periodic boundary conditions in the y and z directions and open boundary conditions in the x direction for meta-atom unit cell calculations. In the present simulations, material absorption is neglected and real-valued refractive indices are used. In realistic devices, both LN and $SiO_2$ exhibit frequency-dependent dispersion and absorption in the THz regime. For reference, room-temperature measurements of LN report THz absorption coefficients of approximately 3.3 and 33.2 $cm^{-1}$ at 0.4 and 1.6 THz, respectively, corresponding to characteristic absorption lengths $1/\alpha$ of about 3.0 and 0.30 mm[49]. These lengths remain more than three orders of magnitude larger than the 132-nm LN resonator thickness, indicating that THz self-absorption within the nanostructure should have a limited effect on the locally generated field. Propagation through a finite $SiO_2$ substrate may nevertheless attenuate the experimentally collected THz amplitude, particularly at higher frequencies. Such common propagation loss is expected to affect the absolute THz output more strongly than the relative LCP-RCP contrast, although frequency-dependent losses may modify the broadband spectrum.

The emitted fields are obtained by solving the time-dependent Maxwell's equations with the nonlinear polarization as the source term. The resulting transient fields are subsequently analyzed via Fourier transform to extract the spectral components across the fundamental, harmonic, and THz regimes. Owing to the symmetry-engineered q-BIC resonances, the local field enhancement becomes intrinsically handedness-dependent (chiral response). This leads to a marked disparity in the nonlinear polarization under LCP versus RCP excitation, ultimately manifesting as chiral THz emission.

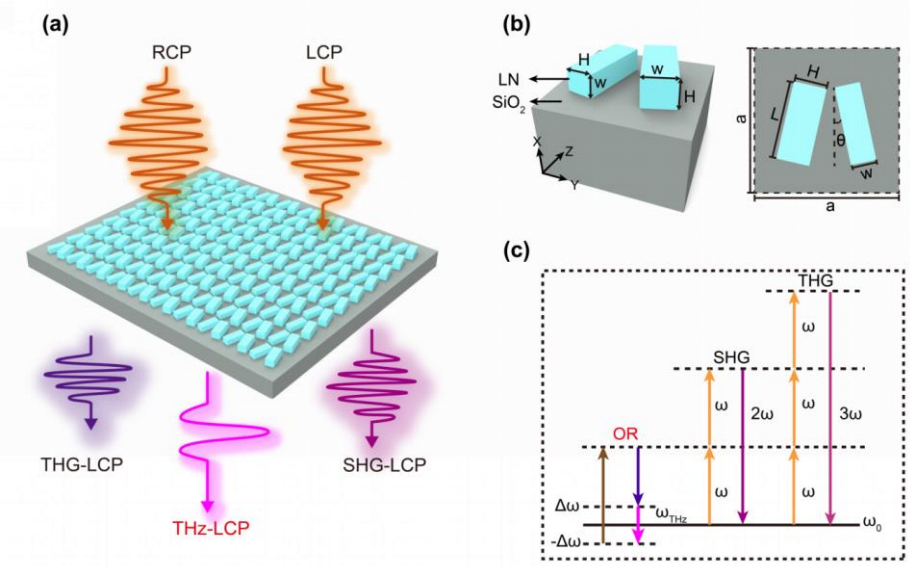



**Fig. 1.** Chiral quasi-BIC metasurface for nonlinear processes. (a) Schematic of the chiral quasi-BIC metasurface with maximized chirality. (b) Schematic and top view of a single unit cell, illustrating the geometric parameters of the LN nanobars: length (L), width (w), height (H), Period (a) and in-plane asymmetry parameter (θ), where L = 310 nm, w = 100 nm, H = 132 nm, a=514 nm and a fixed height difference Δh=H−w =32 nm is maintained. (c) The Energy diagrams illustrating the nonlinear processes of OR, SHG and THG.

## 2.2 Chirality Implementation.

The chiral response of the proposed metasurface is quantified by the transmission CD, defined as

$$CD = \frac{T_{RCP} - T_{LCP}}{T_{RCP} + T_{LCP}} \tag{3}$$

Where $T_{LCP}$ and $T_{RCP}$ denote the transmittance under LCP and RCP illumination, respectively. Figure 2(a) illustrates the evolution of the CD and the quality factor ($Q$-factor) as a function of the in-plane rotation angle $\theta$ with the height disparity fixed at $\Delta h = 32$ nm. As $\theta$ increases, the CD rapidly approaches unity, while the $Q$-factor decreases monotonically. This trend reflects the transition from a symmetry-protected BIC (see Supplementary Note S2) to a radiative q-BIC mode where increased symmetry breaking enhances radiative coupling at the expense of mode confinement. A similar behavior is observed in Fig. 2(b) when varying $\Delta h$ at a fixed $\theta = 12°$ confirming that both in-plane and out-of-plane asymmetries contribute synergistically to chirality generation.

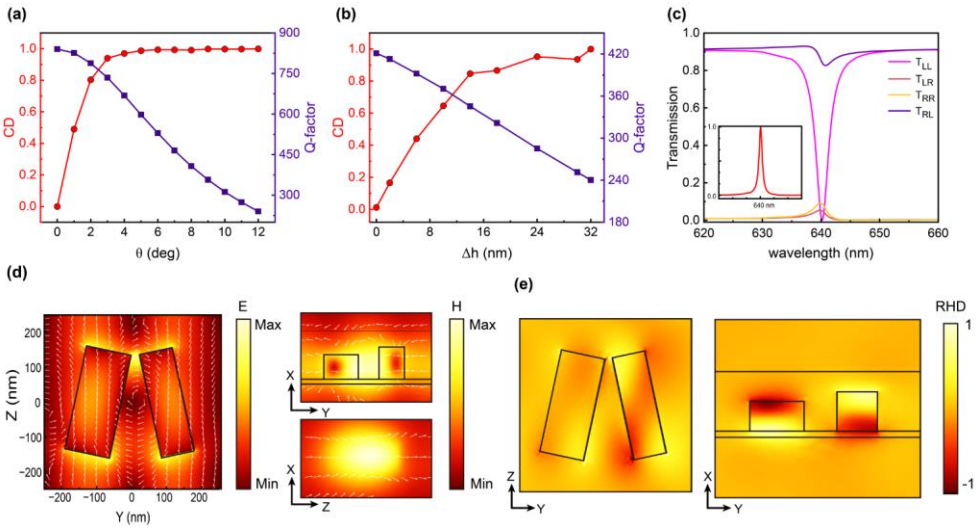



**Fig. 2.** Symmetry-engineered chirality via chiroptical selective q-BIC coupling. (a) CD and $Q$-factor versus in-plane rotation ($\theta$) at fixed $\Delta h = 32$ nm, increasing $\theta$ enhances radiation coupling, yielding higher CD and reduced $Q$-factor. (b) CD and $Q$-factor versus height difference ($\Delta h$): At fixed $\theta = 12°$, showing a similar trade-off driven by out-of-plane symmetry breaking. (c) Chiral-selective transmission spectra: At $\theta = 12°$ and $\Delta h = 32$ nm, the metasurface achieves a near-unity CD ($\approx 0.999$) at 640 nm (d) Near-field distributions reveal asymmetric excitation of the q-BIC mode, with strong localization under LCP and suppressed response under RCP. (e) Reactive helicity density (RHD) reveals an unbalanced chiral near-field induced by simultaneous in-plane and out-of-plane symmetry breaking, consistent with the far-field CD.

The polarization selectivity originates from the interference between the geometric phase introduced by the in-plane rotation $\theta$ and the propagation-induced phase associated with the height difference $\Delta h$[50]. As derived in Supplementary Note S3, the coupling coefficients for the two circular polarization states follow $m_{\pm} \propto sin(k\Delta h/2 \mp \theta)$. Either $\theta$ or $\Delta h$ alone gives identical coupling strengths for the two circular polarizations and therefore cannot produce a chiral response. When both asymmetries are introduced, however, the two coupling coefficients become unequal. Near the destructive-interference condition $k\Delta h/2 \mp \theta \approx 0$, one circular polarization channel is strongly suppressed, whereas the opposite polarization remains resonantly coupled to the BIC mode. For $\theta = 12°$ and $\Delta h = 32$ nm, this interference produces a near-unity linear CD of 0.999 at 640 nm while retaining strong resonant field localization under LCP excitation [Fig. 2(c, d)]. At this wavelength the mode position is dictated by the extraordinary refractive index of the x-cut LN. The corresponding transmission

spectra in Fig. 2(c) exhibit a pronounced resonant dip under LCP excitation, whereas the response under RCP remains suppressed due to the effective decoupling of the q-BIC mode. To characterize the chiral near-field, we evaluate the reactive helicity density[50-52] (RHD), defined as

$$RHD = \frac{c}{\omega} Re(\boldsymbol{D} \cdot \boldsymbol{B}^*) \tag{4}$$

As shown in Fig. 2(e), the simultaneous breaking of the in-plane and out-of-plane symmetries removes the cancellation between oppositely signed local RHD contributions, producing an unbalanced chiral near-field. Here, RHD serves as a near-field indicator of the polarization-selective q-BIC excitation rather than as the nonlinear source itself. The same resonant asymmetry produces a pronounced difference in the locally enhanced $E_z$ field between LCP and RCP. In x-cut LN, the optical-rectification source is dominated by the $d_{33}$-mediated nonlinear polarization driven by $E_z$. The resulting field imbalance is therefore transferred to $P_z^{(2)}$ and ultimately to the generated THz radiation.

The nonlinear response of the proposed LN metasurface is investigated using both transient time-domain simulations and steady-state frequency-domain calculations. Under LCP excitation, the temporal evolution of the electric field (Fig. 3(a)) consists of a prompt transmitted pulse followed by a long-lived resonant tail arising from the q-BIC mode. The sustained oscillations in the resonant tail indicate efficient energy storage and delayed radiative release associate with the high-$Q$ q-BIC resonance[53]. In contrast, the RCP response shown in Fig. 3(c) is dominated by the directly transmitted pulse, while the absence of a pronounced secondary wave packet or resonant tail indicates efficient decoupling from the q-BIC mode. This strong asymmetry between LCP and RCP excitation directly reflects the polarization-selective coupling mechanism established in Fig. 2 and Supplementary Note S3.

The frequency spectrum in Fig. 3(b), obtained via DFT of the transient electric field $E(t)$ in Fig. 3(a) (see Supplementary Note S4), resolves THz radiation, the fundamental frequency (FF), second-harmonic generation (SHG), and third-harmonic generation (THG). The broadband THz response originates from optical rectification, where frequency components within the pulse bandwidth undergo difference-frequency mixing. Although the absolute nonlinear conversion efficiencies obtained from transient and steady-state simulations differ

due to finite cavity-buildup dynamics, both approaches consistently predict strong polarization-selective enhancement, with LCP excitation producing substantially higher nonlinear output than RCP excitation. This agreement confirms the robustness of the underlying q-BIC-mediated chiral nonlinear mechanism (see Supplementary Note S7 and Table S1).

A pronounced enhancement of the nonlinear response is observed in the q-BIC metasurface. Compared with an unpatterned LN thin film, the optimized structure achieves a five-order-of-magnitude enhancement in SHG efficiency under LCP light (Supplementary Note S5). Simultaneously, the SHG efficiency under LCP illumination exceeds that under RCP excitation by nearly two orders of magnitude, yielding a near-unity SHG-CD value of 0.99. This benchmark places the device among the best-performing nonlinear chiral metasurfaces reported to date (see Supplementary Notes S5, S11, and Table S3).

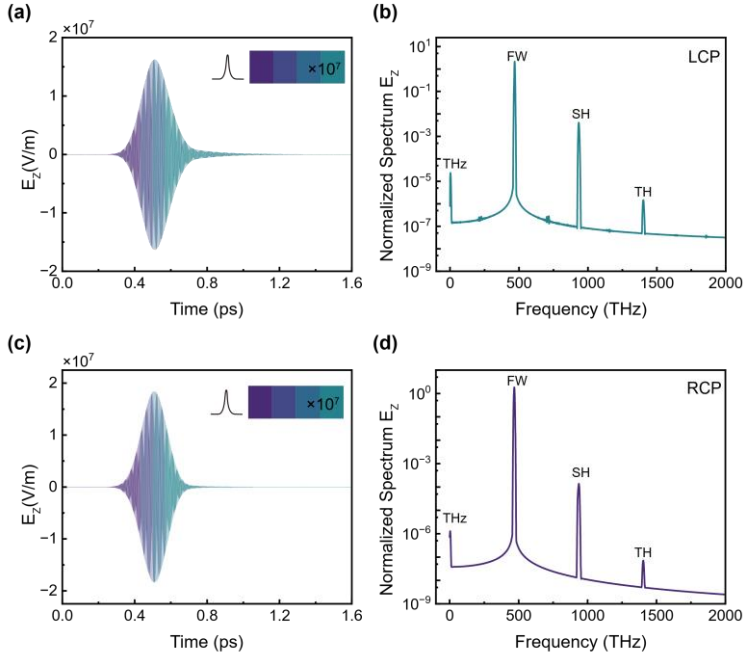



**Fig. 3**. Transient time-domain dynamics and normalized spectral characteristics under chiral excitation. The metasurface consists of LN dimers ($\theta = 12°$, $\Delta h = 32$ nm) illuminated by an ultrafast pulse ($E_0 = 2 \times 10^7$ V/m, $dt = 100$ fs and $t_0 = 0.5$ ps). (a, c) Temporal evolution of $E_z$ under LCP and RCP excitation, showing a prompt transmitted pulse followed by a long-lived resonant tail under LCP excitation, while the resonant tail is strongly suppressed under RCP excitation. (b, d) Normalized frequency spectra scaled against the incident reference pulse, resolving the THz, FF, SHG and THG components.

The THz emission also exhibits similarly strong polarization dependence. As shown in Figs. 3(b) and 3(d), the normalized THz spectral amplitude under LCP excitation reaches $2.4 \times 10^{-5}$, which is comparable to that of previously reported nonlinear metasurface emitters[54]. A broader comparison of THz field strength, generation mechanism, and chiral performance with representative experimental THz sources is provided in Supplementary Note S13 and Table S4. Whereas the corresponding RCP background is strongly suppressed by approximately one order of magnitude. To quantify the broadband chiral purity of the emitted THz radiation, the frequency-dependent terahertz circular dichroism, $THz\text{-}CD(\omega)$, is defined as

$$THz\text{-}CD(\omega) = \frac{I_{LCP}(\omega) - I_{RCP}(\omega)}{I_{LCP}(\omega) + I_{RCP}(\omega)} \quad (5)$$

where $I_{LCP}(\omega)$ and $I_{\mathrm{RCP}}(\omega)$ denote the normalized THz spectral intensities under LCP and RCP excitation, respectively. Beyond the peak THz-CD evaluated at the peak frequency of emitted THz spectrum, the overall chiral performance is further characterized by the full-spectrum averaged THz-CD ($THz\text{-}CD_{avg}$), evaluated over entire simulated THz range of 0-10 THz (Supplementary Note S8 and Table S2).

## 2.3 Geometric Modulation: Balancing THz Efficiency and Chiral Purity.

The effects of the two structural asymmetry parameters, $\Delta h$ and $\theta$, on THz generation and chiral purity are summarized in Fig. 4. The corresponding resonance evolution, THz-CD definition, and extracted spectral parameters are provided in Supplementary Notes S6, S8 and S9, respectively. The corresponding RCP results are presented in Supplementary Note S10. In Fig. 4(a), the THz spectral intensity increases continuously with increasing height difference, whereas the peak frequency and spectral bandwidth remain nearly unchanged. As discussed in Supplementary Note S6, the excitation wavelength is adjusted to track the resonance wavelength of each specific configuration, ensuring efficient resonant excitation throughout the resonance sweep. Consequently, the THz output remains strong despite the gradual reduction of the resonance $Q$-factor.

The evolution of THz chirality reveals a more stringent optimization criterion. As shown in Fig. 4(c), the peak THz-CD reaches approximately 0.96 at $\Delta h = 24\ nm$, whereas the average THz-CD remains limited to about 0.93. Increasing the height difference to 32 nm elevates the

average THz-CD to 0.99, indicating that broadband chiral purity requires a stronger degree of symmetry breaking than single-frequency chirality. Although the maximum THz output is obtained near $\Delta h = 30\ nm$, the $\Delta h = 32$ nm configuration provides a superior balance between THz intensity and broadband chiral performance. A similar trade-off emerges in the $\theta$-dependent study. With $\Delta h = 32\ nm$ fixed, the THz output exhibits a strong dependence on the rotation angle (Fig. 4(b)). The emitted THz intensity increases substantially with increasing $\theta$, while both the peak and average THz-CD increase monotonically and gradually approach saturation. Notably, the average THz-CD already exceeds 0.95 at $\theta = 6°$, indicating that robust chirality can be achieved over a relatively broad parameter range. Further increasing $\theta$ enhances the broadband chiral purity and ultimately drives the average THz-CD to near unity.

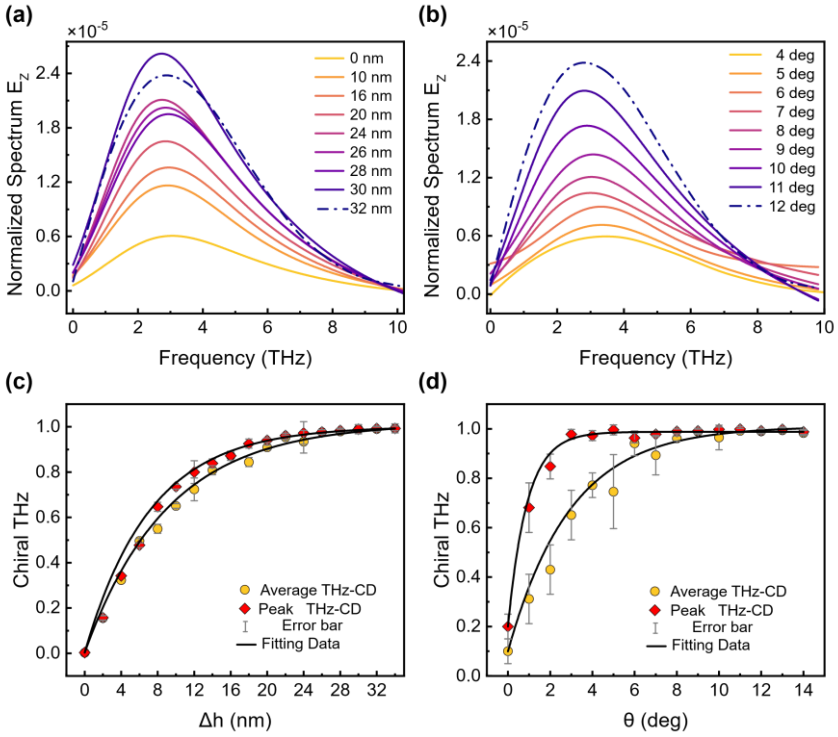



**Fig. 4.** Geometric tuning of THz emission and chirality. (a, b) THz spectra as functions of the height difference $\Delta h$ at a fixed rotation angle of $\theta = 12°$ and the rotation angle $\theta$ at a fixed height difference of $\Delta h = 32$ nm, respectively. (c, d) Evolution of peak and full-spectrum average THz-CD as function of geometric asymmetry. The average THz-CD converges more slowly than the peak THz-CD, indicating that broadband chiral purity requires stronger symmetry breaking. The optimized configuration ($\theta = 12°$, $\Delta h = 32$ nm) simultaneously achieves both maximum THz output and near-unity chirality.

Considering both THz output and chiral purity, the configuration $(\theta, \Delta h) = (12°, 32\ nm)$ is selected as the optimal operating point. This geometry provides a balance between suppressing the undesired circular-polarization coupling channel and preserving strong q-BIC-mediated field enhancement, thereby maintaining an efficient $d_{33}$-dominated optical-rectification source. The resulting combination of polarization-selective coupling and resonant field enhancement accounts for the simultaneously strong THz output and near-unity broadband chirality. From a fabrication perspective, $\theta$ can be lithographically defined, while $\Delta h$ can be introduced through calibrated shallow etching on the LNOI platform[55]. Moreover, the high chiral response persists over a finite parameter range, for example, the average THz-CD remains approximately 0.98 at $\Delta h = 28$ nm compared with 0.99 at 32 nm, indicating reasonable tolerance to moderate fabrication deviations.

## 2.4 Pump Pulse Dynamics and Robustness of Chiral THz Emission.

The excitation pulse duration provides an additional degree of freedom for dynamically controlling the emitted THz spectrum in the optimized structural configuration ($\theta = 12°$, $\Delta h = 32$ nm). Figure 5(a) presents the time-domain THz waveforms generated under LCP excitation for pump pulse widths ranging from 50 to 140 fs. Throughout this pulse-duration sweep, the incident peak electric-field amplitude $E_0$ and beam waist are kept fixed, so that the peak optical intensity and peak power remain unchanged. The emitted signals exhibit a characteristic bipolar profile identifying them as Ricker wavelets (Mexican-hat) profiles[54]. As the pulse duration increases, the temporal waveform broadens and its peak amplitude gradually decreases, while the overall waveform symmetry is preserved.

As shown in Fig. 5(b), increasing the pump pulse width induces a pronounced redshift of the spectral peak, together with progressive spectral narrowing. Since the emitted THz field is proportional to the second temporal derivative of the nonlinear polarization, the time-domain waveform can be expressed as

$$E_{THz}(t) \propto \left(1 - \frac{2t^2}{dt^2}\right) \exp\left(-\frac{t^2}{dt^2}\right) \quad (6)$$

which directly links the THz spectral characteristics to the temporal envelope of the excitation pulse (see Supplementary Note S1).

Quantitative extraction of the spectral features in Fig. 5c reveals that both the peak frequency and the FWHM decrease monotonically with increasing pulse duration. The Fourier transform of Eq. (6) yields $E_{THz}(f) \propto f^2 \exp(-\pi^2 f^2 dt^2)$, form which the scaling laws $f_{peak} = 1/(\pi dt)$ and $FWHM \approx 1.15/(\pi dt)$ [56] are obtained. The excellent agreement between the numerical simulations and theoretical predictions confirms that the THz center frequency and bandwidth can be continuously tailored through pump-pulse engineering.

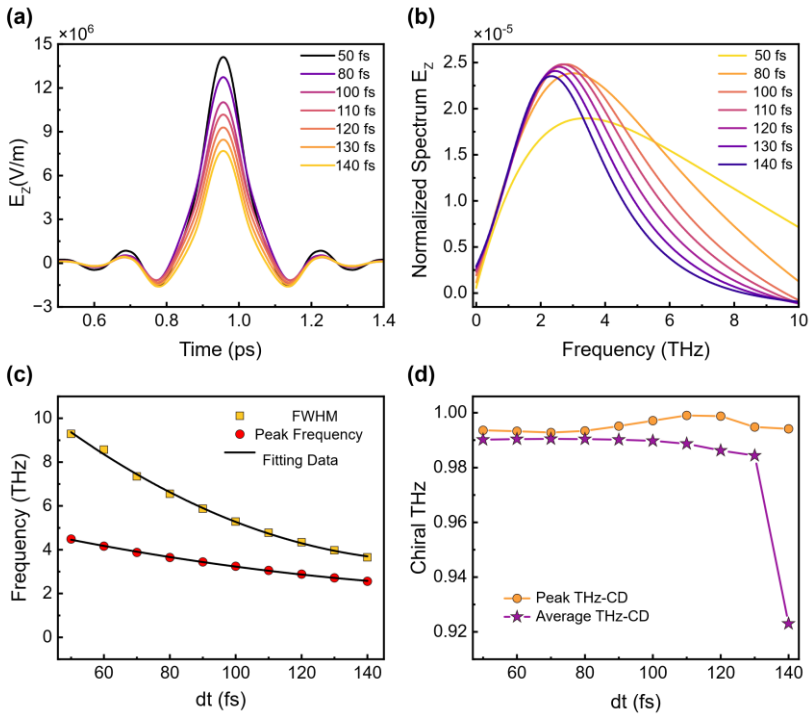



**Fig. 5.** Dynamic control of THz emission through pump pulse widths ($dt$). (a) Time-domain THz waveforms under LCP excitation for pulse durations ranging from 50 to 140 fs. (b) Corresponding THz spectra. (c) Extracted peak frequency and spectral FWHM as a function of $dt$, with solid lines representing numerical fits based on $f_{\text{peak}} = 1/(\pi dt)$ and $FWHM \approx 1.15/(\pi dt)$. (d) Peak THz-CD and average THz-CD versus $dt$.The decrease in average THz-CD at long pulse durations originates from the attenuation of high-frequency chiral spectral components.

As shown in Fig. 5(d), both the peak THz-CD and the full-spectrum averaged THz-CD remain close to unity over a wide range of pulse durations. In particular, under the 100-fs excitation used for the optimized configuration, the frequency-resolved THz-CD remains close to 0.99 throughout the simulated 0–10 THz range, as further confirmed in Supplementary Fig. S6(d). The full-spectrum averaged THz-CD exceeds 0.98 for pulse durations up to 130 fs and remains above 0.92 even at 140 fs. A frequency-resolved analysis reveals that the slight

reduction observed at longer pulse durations originates primarily from the attenuation of high-frequency chiral spectral components (see Supplementary Note S12 and Supplementary Fig. 6(d)). These results demonstrate the exceptional robustness of the q-BIC-mediated chiral emission mechanism against variations in pump-pulse duration.

## 3. Conclusion.

In conclusion, we have theoretically demonstrated a chiral THz emitter based on an asymmetric LN metasurface supporting a chiral q-BIC resonance. The simultaneous breaking of in-plane and out-of-plane symmetries enables near-unity THz CD (≈ 0.99) and strongly enhanced nonlinear THz emission. The underlying structural chirality is further corroborated by the pronounced polarization selectivity observed in both the linear response and second-harmonic generation. The platform further supports dynamic spectral tuning via pump-pulse engineering while maintaining high chiral purity over the dominant THz emission band. The proposed symmetry-engineering strategy is not restricted to LN and can, in principle, be extended to other $\chi^{(2)}$ dielectric platforms supporting suitable q-BIC resonances and nonlinear tensor components. This general framework provides a scalable route toward integrated chiral THz sources for sensing, spectroscopy, and communication applications.

**Acknowledgement:** This work was supported by the Key Program of National Natural Science Foundation of China, Grant Nos.12332002. This work was also supported by the Program of China Scholarship Council (Grant No. 202407810013).

# References:

[1] Tang YandCohen A E **2011** *Sci 332* 333

[2] Koshelev K,Tonkaev PandKivshar Y **2023** *Adv. Photonics 5* 064001

[3] Sharma V,Mishra A K,Mishra N KandVinod **2025** *Chirality 37* e70057

[4] Valev V K,Baumberg J J,Sibilia CandVerbiest T **2013** *Adv. Mater. 25* 2517

[5] Ayuso D,Neufeld O,Ordonez A F,Decleva P,Lerner G,Cohen O,Ivanov MandSmirnova O **2019** *Nat. Photon. 13* 866

[6] Wang R,Zhang D,Chen L,Zhang N,Li D,Jiang R,Zhang X,Yang X,Zhang L,Wang S,Liu X,Chang CandTsai D P **2025** *Nat. Commun. 16* 11462

[7] Zhang S,Zhu S,Tian S,Zhang L,Chen C,Xiao K,Mo W,Hou S,Zhang Y,Wen Y,Tan Y,Zhang K,Han J,Liu C,He J,Tang W,Wang J,Li G,Zhang K,Wang LandChen X **2026** *Light Sci. Appl. 15* 100

[8] Ukirade N A **2025** *Next Mater. 6* 100479
[9] Makhlouf S,Cojocari O,Hofmann M,Nagatsuma T,Preu S,Weimann N,Hübers H-WandStöhr A **2023** *IEEE J. Microw. 3* 894
[10] Ahmed S,Alam T,Soliman M M,Moubark A M,Rahman M M,Islam M SandIslam M T **2025** *Sci. Rep. 15* 22996
[11] Xu S-T,Fan J,Xue Z,Sun T,Li G,Li J,Lu DandCong L **2024** *Photonics Res. 12* 2207
[12] Zhang Z,Chen Y,Cui S,He F,Chen M,Zhang Z,Yu J,Chen L,Sheng ZandZhang J **2018** *Nat. Photon. 12* 554
[13] Li J-H,Xiong H-T,Kong D-Y,Zhao W-P,Liu S-J,Quan B-GandWu X-J **2024** *Chin. Phys. Lett. 41* 124201
[14] Wang S,Liu C,Zhang S,Cai Q,Wang P,Tian C,Zhou L,Wu YandTao Z **2023** *2022 CLEO San Jose CA USA pp1*
[15] Xi Y,Zhou Y,Liang X,Cao X,Wu Y,Xu G,Zhang Y,Shi W,Huang YandXu X **2026** *Adv. Funct. Mater. 0* e21708
[16] Zhou C,Liu Y P,Wang Z,Ma S J,Jia M W,Wu R Q,Zhou L,Zhang W,Liu M K,Wu Y ZandQi J **2018** *Phys. Rev. Lett. 121* 086801
[17] Seifert T,Jaiswal S,Martens U,Hannegan J,Braun L,Maldonado P,Freimuth F,Kronenberg A,Henrizi J,Radu I,Beaurepaire E,Mokrousov Y,Oppeneer P M,Jourdan M,Jakob G,Turchinovich D,Hayden L M,Wolf M,Münzenberg M,Kläui MandKampfrath T **2016** *Nat. Photon. 10* 483
[18] Zhang B,Ma Z,Ma J,Wu X,Chen O,Kong D,Hong T,Wang X,Yang P,Chen L,Li YandZhang J **2021** *Laser Photon. Rev. 15* 2000295
[19] Jolly S W,Matlis N H,Ahr F,Leroux V,Eichner T,Calendron A-L,Ishizuki H,Taira T,Kärtner F XandMaier A R **2019** *Nat. Commun. 10* 2591
[20] Xu A-J,Li J-H,Kong D-Y,Cai J-H,Chen T,Suthar D,Cao P-C,Yu X-Q,Yang Y-L,Zhang M-X,Moutaouakil A EandWu X-J **2025** *Chin. Phys. Lett. 42* 120406
[21] Wang Q,Zhang X,Xu Q,Feng X,Lu Y,Niu L,Chen X,Plum E,Gu J,Yang Q,Fang M,Huang Z,Zhang S,Han JandZhang W **2023** *Adv. Funct. Mater. 33* 2300639
[22] Sideris S,Minerbi E,Mcdonnell CandEllenbogen T **2022** *ACS Photon. 9* 3981
[23] Peters L,Rocco D,Olivieri L,Arregui Leon U,Cecconi V,Carletti L,Gigli C,Della Valle G,Cutrona A,Totero Gongora J S,Leo G,Pasquazi A,De Angelis CandPeccianti M **2024** *Adv. Opt. Mater. 12* 2303148
[24] Sideris S,Z H,Mcdonnell C,Li GandEllenbogen T **2023** *ACS Photon. 10* 2972
[25] Yang J H,Huang Z T,Maksimov D N,Pankin P S,Timofeev I V,Hong K B,Li H,Chen J W,Hsu C Y,Liu Y Y,Lu T C,Lin T R,Yang C SandChen K P **2021** *Laser Photon. Rev. 15* 2100118
[26] Zhong H,He T,Meng YandXiao Q **2023** *Materials 16* 7112
[27] Hsu C W,Zhen B,Stone A D,Joannopoulos J DandSoljačić M **2016** *Nat. Rev. Mater. 1* 16048
[28] Huang Z,Wang M,Li Y,Shang J,Li K,Qiu W,Dong J,Guan H,Chen ZandLu H **2021** *Nanotechnol. 32* 325207
[29] Liu Z,Xu Y,Lin Y,Xiang J,Feng T,Cao Q,Li J,Lan SandLiu J **2019** *Phys. Rev. Lett. 123* 253901
[30] Zhang X,He L,Gan X,Huang X,Du Y,Zhai Z,Li Z,Zheng Y,Chen X,Cai YandAo X **2022** *Laser Photon. Rev. 16* 2200031
[31] Kang L,Bao HandWerner D H **2021** *Opt. Lett. 46* 633
[32] Gandolfi M,Tognazzi A,Rocco D,De Angelis CandCarletti L **2021** *Phys. Rev. A 104* 023524
[33] Chen Y,Deng H,Sha X,Chen W,Wang R,Chen Y H,Wu D,Chu J,Kivshar Y S,Xiao SandQiu C W **2023** *Nature 613* 474

[34] Voronin K,Taradin A S,Gorkunov M VandBaranov D G **2022** *ACS Photon. 9* 2652
[35] Shi T,Deng Z L,Geng G,Zeng X,Zeng Y,Hu G,Overvig A,Li J,Qiu C W,Alù A,Kivshar Y SandLi X **2022** *Nat. Commun. 13* 4111
[36] Liu W,Wang B,Zhang Y,Wang J,Zhao M,Guan F,Liu X,Shi LandZi J **2019** *Phys. Rev. Lett. 123* 116104
[37] Guo X,Lv J,Liu C,Yu Q,Shi J,Liu Q,Wang J,Liu WandChu P K **2026** *Chin. Phys. B 35* 067801
[38] Tonkaev P,Toftul I,Lu Z,Qin H,Qiu S,Yang W,Koshelev K,Lu YandKivshar Y **2024** *Nano Lett 24* 10577
[39] Lai F,Yin J,Toftul I,Barkaoui H,Deng H,Sha X,Gorkunov M V,Kivshar YandSong Q **2025** *Nat. Commun. 16* 10686
[40] Wu X,Hao Z,Bo F,Zhang GandXu J **2022** *Chin. Sci. Bull. 67* 3915
[41] Li G L,Jia Y CandChen F **2020** *Acta Phys. Sin. 69* 157801
[42] Boes A,Chang L,Langrock C,Yu M,Zhang M,Lin Q,Loncar M,Fejer M,Bowers JandMitchell A **2023** *Sci 379* eabj4396
[43] Lin J,Bo F,Cheng YandXu J **2020** *Photonics Res. 8* 1910
[44] Qi YandLi Y **2020** *Nanophoton. 9* 1287
[45] He J,Chen H,Pan K,Su Y,Zhang X,Li W,Zhu S-NandHu X **2024** *ACS Photon. 11* 4111
[46] Wang W,Ju Y,Han Z,Liu JandZhang Y **2025** *Braz. J. Phys. 55* 177
[47] Liu T,Qiu J,Qin M,Tu X,Qiu H,Wu F,Yu T,Liu QandXiao S **2026** *Opto-Electron. Adv. 9* 250257
[48] Shoji I,Kondo T,Kitamoto A,Shirane MandIto R **1997** *J. Opt. Soc. Am. B 14* 2268
[49] Wu X J,Zhou C,Wenqian Ronny Huang,Frederike AhrandKärtner F X **2015** *Opt. Express 23* 29729
[50] Luo C,Hu N,Li J,Hu S,Fu Z,Yu Z,Hou Y,Jin A,Quan B,Tian S,Yang H,Li G,Zhang X,Fan X,Guo YandGu C **2025** *Appl. Phys. Lett. 126* 201705
[51] Deng Q,Li X,Hu M,Li F,Li XandDeng Z **2024** *npj Nanophoton. 1* 20
[52] Chen W,Wang Z,Gorkunov M V,Qin J,Wang R,Wang C,Wu D,Chu J,Wang X,Kivshar YandChen Y **2024** *Nano Lett. 24* 9643
[53] Xia J,Liu J,Liu Y,Liu Z,Wei XandSong G **2026** *Nanophoton. 15* e70104
[54] Fang M,Niu K,Huang Z,Sha W E I,Wu X,Koschny TandSoukoulis C M **2018** *Opt. Express 26* 14241
[55] Zhu D,Shao L,Yu M,Cheng R,Desiatov B,Xin C J,Hu Y,Holzgrafe J,Ghosh S,Shams-Ansari A,Puma E,Sinclair N,Reimer C,Zhang MandLončar M **2021** *Adv. Opt. Photon. 13* 242
[56] Wang Y **2015** *Geophys. 80* A31